crystals

MDPI

Article

Utilizing High-Capacity Spinel-Structured High-Entropy Oxide $(CrMnFeCoCu)_3O_4$ as a Graphite Alternative in Lithium-Ion Batteries

Lenka Oroszová [1], Dávid Csík [1,2], Gabriela Baranová [2], Gábor Bortel [3], Róbert Džunda [1], László Temleitner [3], Mária Hagarová [2], Ben Breitung [4] and Karel Saksl [1,2,*]

[1] Institute of Materials Research, Slovak Academy of Sciences, Watsonova 47, 040 01 Košice, Slovakia; loroszova@saske.sk (L.O.); dcsik@saske.sk (D.C.)
[2] Institute of Materials and Quality Engineering, Faculty of Materials, Metallurgy and Recycling, Technical University of Košice, Letná 9, 042 00 Košice, Slovakia
[3] Institute for Solid State Physics and Optics, HUN-REN Wigner Research Centre for Physics, Konkoly-Thege Miklós út 29-33., H-1121 Budapest, Hungary; bortel.gabor@wigner.hu (G.B.); temleitner.laszlo@wigner.hu (L.T.)
[4] Institute of Nanotechnology, Karlsruhe Institute of Technology (KIT), Hermann-von-Helmholtz-Platz 1, 76344 Eggenstein-Leopoldshafen, Germany
* Correspondence: karel.saksl@tuke.sk

Abstract: In the realm of advanced anode materials for lithium-ion batteries, this study explores the electrochemical performance of a high-entropy oxide (HEO) with a unique spinel structure. The equiatomic composition of CrMnFeCoCu was synthesized and subjected to a comprehensive materials characterization process, including X-ray diffraction and microscopy techniques. The multicomponent alloy exhibited a multiphase structure, comprising two face-centered cubic (FCC) phases and an oxide phase. Upon oxidation, the material transformed into a spinel oxide with a minor presence of CuO. The resulting high-entropy oxide demonstrated excellent electrochemical behavior when utilized as an anode material. Cyclic voltammetry revealed distinctive reduction peaks attributed to cation reduction and solid electrolyte interphase (SEI) layer formation, while subsequent cycles showcased high reversibility. Electrochemical impedance spectroscopy indicated a decrease in charge transfer resistance during cycling, emphasizing the remarkable electrochemical performance. Galvanostatic charge/discharge tests displayed characteristic voltage profiles, with an initial irreversible capacity attributed to SEI layer formation. The HEO exhibited promising rate capability, surpassing commercial graphite at higher current densities. The battery achieved 80% (275 mAh g^{-1}) of its initial stable capacity at a current density of 500 mA g^{-1} by the 312th cycle. Post-mortem analysis revealed structural amorphization during cycling, contributing to the observed electrochemical behavior. This research highlights the potential of HEOs as advanced anode materials for lithium-ion batteries, combining unique structural features with favorable electrochemical properties.

Keywords: lithium-ion battery; anode material; high-entropy oxide; spinel structure

Citation: Oroszová, L.; Csík, D.; Baranová, G.; Bortel, G.; Džunda, R.; Temleitner, L.; Hagarová, M.; Breitung, B.; Saksl, K. Utilizing High-Capacity Spinel-Structured High-Entropy Oxide $(CrMnFeCoCu)_3O_4$ as a Graphite Alternative in Lithium-Ion Batteries. *Crystals* **2024**, *14*, 218. https://doi.org/10.3390/cryst14030218

Academic Editor: Faxing Wang

Received: 31 January 2024
Revised: 20 February 2024
Accepted: 22 February 2024
Published: 24 February 2024

1. Introduction

Our planet is confronted with pressing environmental concerns, including climate change, deforestation, and ozone depletion. Internal combustion engine vehicles are a significant source of carbon dioxide emissions, which contribute to these issues. Electrifying vehicles and harnessing renewable energy sources are crucial steps in addressing the environmental crisis. Energy storage systems play an essential role in optimizing the utilization of renewable energy sources, with advanced batteries and grid-scale storage facilities facilitating the efficient storage and distribution of renewable energy. While lithium-ion batteries reign as the leading technology for electric vehicles and other energy storage applications, they encounter challenges, such as the growing demand for extended-range vehicles and

the necessity for increased energy density and efficiency. However, graphite, the most common anode material in lithium-ion batteries, has a relatively low capacity (372 mAh g^{-1}) and poor high-current performance [1]. Alternative anode materials are being investigated to overcome these limitations. Silicon and tin alloys have high theoretical capacities, but they undergo chemical reactions with lithium during charge–discharge cycles, which can lead to structural changes and capacity degradation [2]. Conversion materials, such as transition metal oxides, are being evaluated for use in the fourth generation of lithium-ion batteries due to their high specific capacity (700–1000 mAh g^{-1}) [3–5]. However, they face similar challenges to alloying materials, such as large volume changes during charging and discharging, which can lead to capacity fading.

High entropy materials diverge from conventional materials due to their unique composition and structure, leading to remarkable functional properties [6–10]. These materials, encompassing multiple essential elements, exhibit distinctive characteristics such as dielectric, optical, magnetic, and electrochemical properties. In the domain of lithium-ion batteries [11–29], high-entropy oxides (HEOs) have demonstrated promise as both anode and cathode materials. Their appeal stems from their ability to deliver high capacities and extended cycle life. The exceptional electrochemical properties stem from the "cocktail effect" arising from diverse atomic sizes and high entropy. In lithium-ion batteries, high-entropy oxides augment electrodes by elevating energy storage capacity and stability throughout charge and discharge cycles. The disorder in their atomic structure, attributable to diverse elements, facilitates efficient lithium-ion diffusion and storage. By harnessing these qualities, HEOs possess the potential to revolutionize energy storage, satisfying the demand for higher energy density, faster charging, and enhanced sustainability.

Among the most extensively investigated HEOs for anode in lithium-ion batteries (LIBs) is a mixed-metal oxide, (MgCoNiCuZn)O with a rock–salt structure. It boasts a theoretical capacity of 700–1000 mAh g^{-1}, two–three times greater than commercial LIB anode materials [11–13]. In this composition, Mg^{2+} acts as a stabilizing element due to its inactivity within the potential range of 0–3 V vs. Li/Li^{+}. This inactivity contributes to stabilizing the crystal structure, inhibiting active nanograin agglomeration, and enhancing cyclic stability [11–13]. However, the incorporation of inactive Mg in high-entropy oxides generally decrease the attainable capacity, as confirmed in [21,30]. Another promising HEO anode material is $(CrMnFeCoNi)_3O_4$, which possesses a spinel structure [15–18]. During galvanostatic cycling [17], it exhibits a remarkable discharge capacity of 1235 mAh g^{-1} at a current density of 100 mA g^{-1}, accompanied by a Coulombic efficiency that exceeds 99%. Additionally, a remarkable 500 mAh g^{-1} capacity at 2000 mA g^{-1} was achieved during rate capability testing. Nguyen et al. [22] synthesized a Co-free high-entropy oxide $(CrMnFeNiCu)_3O_4$ with outstanding rate capability and stability that exceeds 99% of CE. Chen et al. [19] prepared $(MgTiFeCuZn)_3O_4$ high-entropy oxides via a simple solid-state method, achieving a high specific capacity of 279 mAh g^{-1} at 2000 mA g^{-1} for 800 cycles. The stabilization effect in spinel-structured high-entropy oxides can be achieved by incorporating Ti and/or Al into the HEOs' crystal structure, as demonstrated in [26,28].

The most widely studied high-entropy oxide with spinel structure in lithium-ion batteries is $(CrMnFeCoNi)_3O_4$ [15–18,31,32], but a plenty of derivatives of this HEO have been employed in lithium-ion batteries, such as $(CrMnFeNiZn)_3O_4$ [21], $(CrMnFeCoZn)_3O_4$ [33], $(CrMnFeNiMg)_3O_4$ [21], $(CrMnFeCoMg)_3O_4$ [30], and $(CrMnFeNiCu)_3O_4$ [22,34,35], showcasing the remarkable adjustability/tunability of LIB properties through HEO composition. However, to the best of our knowledge, no study has yet explored the application of $(CrMnFeCoCu)_3O_4$ high-entropy oxide in lithium-ion batteries. Consequently, we synthesized $(CrMnFeCoCu)_3O_4$ high-entropy oxide by oxidizing the multicomponent pre-alloy powder particles at elevated temperatures. The prepared high-entropy oxide was utilized in lithium-ion half cells and compared to a traditional graphite electrode. The microstructure and phase evaluation of the alloy, oxide, and electrodes, including post-mortem analysis, was examined using scanning electron microscopy and X-ray diffraction, respectively.

2. Materials and Methods

2.1. Materials Synthesis

The multicomponent pre-alloy of CrMnFeCoCu in equiatomic composition was synthesized by arc melting of pure elements of Cr, Mn, Fe, Co, and Cu (>99.9%, Thermo Fisher, Kandel, Germany) in an argon atmosphere. The samples were remelted five times in a water-cooled copper mold using a Bühler Compact Arc Melter MAM-1 (Edmund Bühler GmbH, Bodelshausen, Germany). After each melting, the samples were turned over to ensure homogeneous composition throughout the entire volume. The samples were then milled in a vibration mill at a frequency of 30 Hz for 1 h and sieved to a size of less than 40 μm. The resulting powder particles of the alloy were oxidized in a tube furnace (LAC L HR, LAC, Židlochovice, Czech Republic) under an oxygen atmosphere at 1000 °C for a duration of 6 h. The oxidized powder was rapidly quenched on a steel plate. Further refinement was carried out through milling in a planetary ball mill (Retsch PM 100, Retsch GmbH, Haan, Germany) using tungsten carbide balls with a diameter of 10 mm. The milling process occurred at a rotational speed of 500 rpm for 30 min in isopropanol. Finally, the milled powder was dried at 70 °C and used for material characterization and utilization in electrochemical cells.

2.2. Materials Characterization

X-ray diffraction (XRD) was utilized for assessing the phase purity of the prepared materials. A Huber G670-360 Guinier Imaging Plate Camera (Huber Diffraktionstechnik GmbH & Co. KG, Rimsting, Germany) equipped with a Mo anode X-ray tube source was employed. Diffractograms were captured in the 0–100° scattering angle range at ambient temperature. Mo $K\alpha_1$ radiation (λ = 0.70926 Å) was selected using a focusing Ge 220 Johannson monochromator (Huber Diffraktionstechnik GmbH & Co. KG, Rimsting, Germany). For measurements in asymmetric transmission geometry, the powder samples were mounted on a 6.0 μm thick mylar thin film. To enhance powder averaging, an in-plane oscillating motion of the sample was applied. Each measurement was conducted with an exposure of 1 h. The powder diffraction patterns were analyzed and refined using GSAS-II software (Argonne National Laboratory, Lemont, IL, USA) (Version V5556) [36,37]. The microstructure of the bulk alloy was evaluated using Jeol JSM 7000 F Scanning electron microscopy (SEM) (JEOL, Tokyo, Japan) equipped with energy-dispersive spectroscopy (EDS) Oxford Inca X-sight model 7557 (Oxford Instruments, High Wycombe, UK). Scanning electron microscopy was conducted with a Tescan VEGA 3 LME instrument (TESCAN, Brno, Czech Republic) equipped with energy-dispersive X-ray spectroscopy (Bruker, Billerica, MA, USA) to analyze the morphology, size distribution, and chemical composition of the prepared powder materials and electrodes before and after cycling. Post-mortem XRD on the electrodes was utilized to investigate phase transformation during the cycling process using a Philips X'Pert Pro diffractometer (Philips, Amsterdam, The Netherlands) operating in Bragg–Brentano (reflection) mode at 40 kV and 50 mA, employing Cu Kα radiation (λ= 1.5418 Å).

2.3. Electrochemical Measurements

Electrochemical measurements were performed using CR2032 coin cells. The prepared high-entropy oxide (70 wt.%) was blended with Super P carbon black (20 wt.%) and polyvinylidene fluoride (PVDF) (10 wt.%) dissolved in N-methyl pyrrolidone (NMP). Mixing was performed in a planetary centrifugal mixer (Thinky ARE-250, Tokyo, Japan) to form a slurry for 20 min, including a degassing step. The slurry was coated onto a copper foil using a Compact Tape Casting Coater (MTI MSK-AFA-III, MTI, Richmond, VA, USA), resulting in a wet film height of 120 μm. The coated foil was dried at 120 °C under vacuum overnight. Electrodes with a diameter of 13 mm were cut from the prepared coated foil using EL-Cut (EL-CELL, Hamburg, Germany) with a material loading of approximately 1.64 mg cm^{-2}. The half cells were assembled in an argon-filled glovebox (Jacomex GP Campus) (Jacomex, Dagneux, France) maintained at a controlled atmosphere (O_2 < 1 ppm,

$H_2O < 1$ ppm). Li discs (13 mm in diameter) served as counter electrodes, the HEO electrode as the working electrode, Whatman GF/A was employed as the separator, and 1 M $LiPF_6$ dissolved in ethyl carbonate (EC) and diethyl carbonate (DEC) in a 50/50 volume ratio was used as the electrolyte. Cyclic voltammetry at a sweep rate of 0.1 mV s^{-1} in a potential range of 0.01 to 3 V and electrochemical impedance spectroscopy (EIS) in a frequency range of 1 MHz to 100 mHz were conducted using a potentiostat/galvanostat (BioLogic SP-150, Biologic, Seyssinet-Pariset, France). Galvanostatic charge–discharge tests at various current densities in a potential range of 0.01 to 3 V were performed using a Landt Battery Cycler (CT3002AU, Landt Instrument, New York, NY, USA).

3. Results and Discussion

3.1. Material Characterization

To analyze the phase composition of the synthetized multicomponent alloy, an XRD experiment was conducted on the powder sample (Figure 1a). The alloy exhibited a multiphase structure, with two face-centered cubic (FCC) phases belonging into the space group of Fm−3m with lattice parameters of a = 3.641 Å (Fm−3m_1) and a = 3.710 Å (Fm−3m_2) in a ratio of 2:1. SEM micrographs of the bulk HEA using back-scattered electrons and EDS analysis indicate that the bright regions were mainly composed of Cu (70.61 at.%) and Mn (24.07 at.%) (Figure 1c,d, Table 1), while the dark regions consisted of nearly equiatomic Cr, Fe, and Co, with a small amount of Mn and low Cu content (Figure 1c,d, Table 1). Considering the lattice parameter of Cu (3.614 Å), we assume that the bright phase (rich in Cu) corresponds to phase 1 (3.641 Å), and the dark phase to phase 2 (3.710 Å). However, an additional phase was also observed, which we were not able to identify (Figure 1a,c,d). EDS analysis revealed that this phase was composed primarily of O, Cr, and Mn, suggesting the presence of an oxide phase. In a previous study by Otto et al. [38], the microstructure of a high-entropy alloy with the same composition was analyzed. However, the alloy in that study was annealed for 3 days at 1123 K, resulting in the formation of two FCC phases, one of which was enriched in Cu and Mn, as in our case. In other studies [38,39], the tertiary phase was assumed to be a sigma phase. However, the sigma phase is an intermetallic compound, unlike the additional phase we observed. As our primary focus was on the high-entropy oxide material, we did not conduct further investigation of this phase. The SEM analysis revealed that the milled particles exhibited deformed shapes, ranging in size from a few hundred nanometers to approximately 40 µm (Figure 1b). EDS analysis confirmed that the constituent elements were homogeneously distributed across the analyzed area, with no evidence of segregation (Figure 1b). However, in some regions, the iron concentration was slightly elevated due to contamination from the milling process. Although this minor contamination is negligible, it is worth noting. The chemical composition of the prepared alloy was nearly equiatomic (Table 2). The configurational entropy ΔS of the prepared multicomponent alloy was calculated separately for each phase, excluding the oxide phase (Table 1). According to [40,41], this multicomponent alloy does not belong to entropy-stabilized alloys due to its high formation enthalpy [42].

Table 1. EDS analysis of multicomponent alloy bulk sample.

Phases	O (at.%)	Cr (at.%)	Mn (at.%)	Fe (at.%)	Co (at.%)	Cu (at.%)	ΔS
Bright phase (B)	-	1.22	24.07	1.52	2.59	70.61	0.81 R
Dark phase (D)	-	24.16	16.19	27.77	27.46	4.43	1.49 R
Dark phase in dark phase (DD)	-	36.33	14.78	26.50	20.34	2.05	1.41 R
Oxide phase	56.00	26.94	14.63	0.18	-	2.26	-

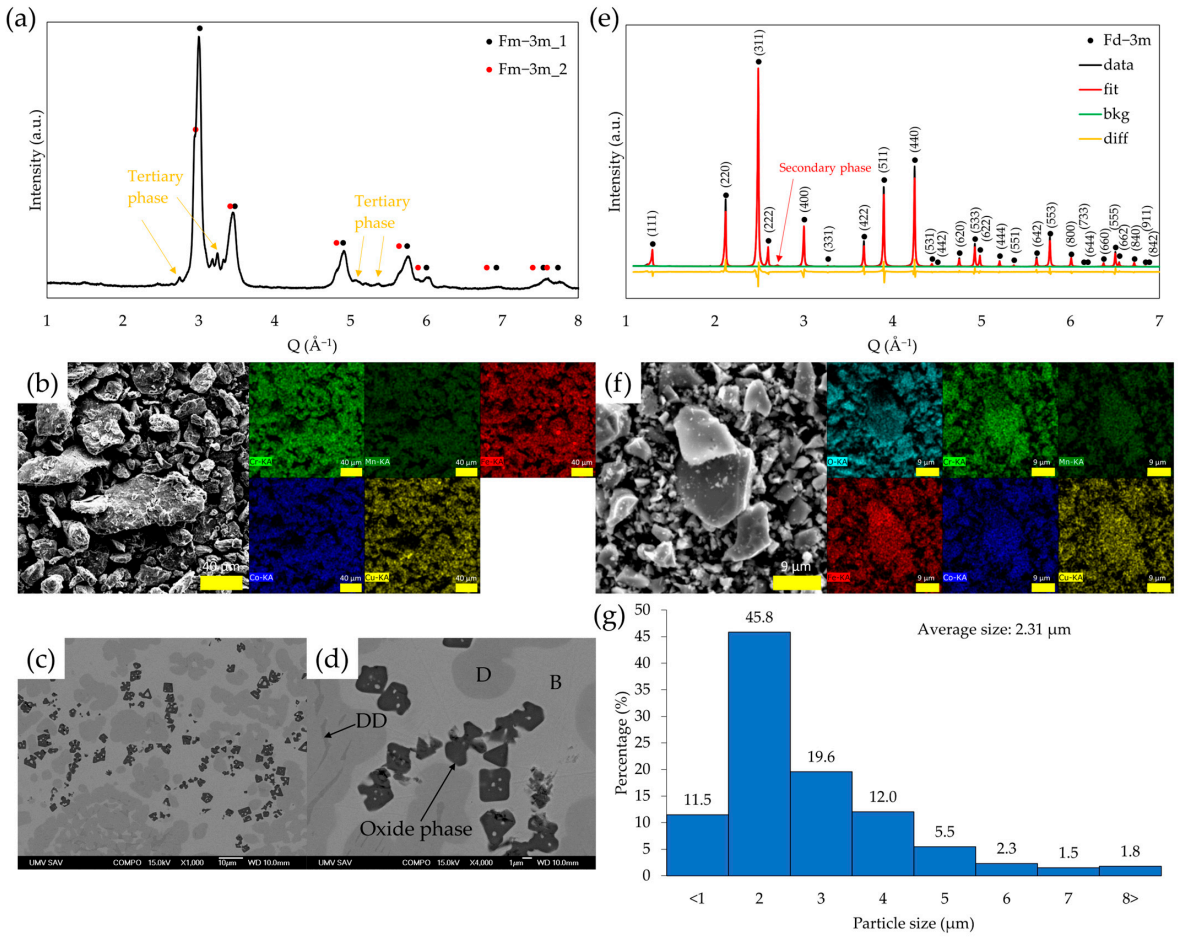

Figure 1. (**a**) XRD phase analysis of the alloy powder; (**b**) EDS mapping of the alloy powder; (**c**,**d**) microstructure of the bulk alloy; (**e**) Rietveld refined XRD pattern of HEO powder, Rwp = 9.3%; (**f**) EDS mapping of HEO powder; (**g**) size distribution of HEO powder.

Table 2. EDS analysis of the alloy powder and HEO powder.

Material	O (at.%)	Cr (at.%)	Mn (at.%)	Fe (at.%)	Co (at.%)	Cu (at.%)
Multicomponent alloy	7.55	18.60	19.22	19.54	17.99	17.10
HEO	60.82	7.12	7.13	8.69	8.28	7.96

During the oxidation of the prepared alloy, a phase transformation occurred, as revealed by XRD analysis of the sintered powder material (Figure 1e). The prepared material belonged to the spinel oxide group, crystallizing in the Fd−3m space group with a lattice parameter of 8.358 Å. However, a small amount of a secondary phase (0.9 wt.%) was observed, exhibiting a monoclinic structure with C2/c space group and lattice parameters of a = 4.688 Å, b = 3.494 Å, c = 5.070 Å, and β = 100.954°. These parameters suggest that the secondary phase is based on CuO. In contrast to other studies [43], which report a single-phase spinel structure for this composition, the authors employed a hydrothermal synthesis route followed by calcination at a low temperature of 700 °C. According to other works [29,38,44], copper can segregate at high temperatures (above 1212 K, 939 °C) and form CuO separately from other oxides during slow cooling processes. Liu et al. [45] observed similar CuO segregation when preparing HEO with a similar composition of CrFeCoNiCu. However, the amount of CuO in their study was 21.5%. This indicates that Mn may have a stronger stabilizing effect on the spinel structure than Ni, even though the HEO precursor in [45] was calcinated at 700 °C. Nevertheless, the small amount of CuO

observed in our work can be considered negligible. SEM analysis revealed that the size distribution of the prepared high-entropy oxide ranged from a few hundred nanometers to approximately 21 µm (Figure 1f). The average particle size was around 2.31 µm (Figure 1g). The chemical composition of the prepared HEO was found to be in good agreement with the theoretical value of Me_3O_4 (Table 2). Based on the analyzed chemical composition, suggesting that all elements occupy both Wyckoff sites for the cations, the calculated configurational entropy of the prepared HEO is approximately 1.99 R, classifying it as a high-entropy material according to [40,41]. These results suggest successful synthesis of the high-entropy oxide, providing a basis for further electrochemical investigation.

3.2. Electrochemical Performance

3.2.1. Cyclic Voltammetry

The electrochemical performance of the prepared high-entropy oxide $(CrMnFeCoCu)_3O_4$ was investigated in half cells with metallic lithium as the counter electrode and a typical electrolyte 1 M $LiPF_6$ in EC/DEC (50/50 v/v). Cyclic voltammetry (CV) was conducted in the potential range of 0.01 V to 3 V vs. Li/Li^+ at a sweep rate of 0.1 mV s^{-1}, as illustrated in Figure 2a. In the first cycle, a sharp reduction peak at 0.5 V is observed attributed to the reduction in cations similar to other compositions [17,22,27,29,46]. Another reduction at 0.25 V is associated with the formation of the solid electrolyte interphase (SEI) layer due to electrolyte degradation [15–17,20,29]. It is noteworthy that the particle size, controlled by the preparation method and parameters, influences the shape of the CV curve, as discussed in previous studies [22]. During the subsequent anodic process, a broad oxidation peak is observed in the potential range of 1.2 and 2.2 V indicative of the oxidation of the metallic phases [15,27,29,30,46]. In the subsequent cycles, the two reduction peaks shifted to higher potentials of 0.47 and 0.90 V, respectively, a common observation in high-entropy oxides (HEOs) [15–17,29]. This shift indicates a large irreversible reaction in the first cycle. However, in subsequent cycles, the CV curves exhibited similar shapes, and with increasing cycle numbers, they tend to overlap, demonstrating high cycle stability and reversibility. This suggests promising electrochemical performance for the $(CrMnFeCoCu)_3O_4$ high-entropy oxide in lithium-ion batteries.

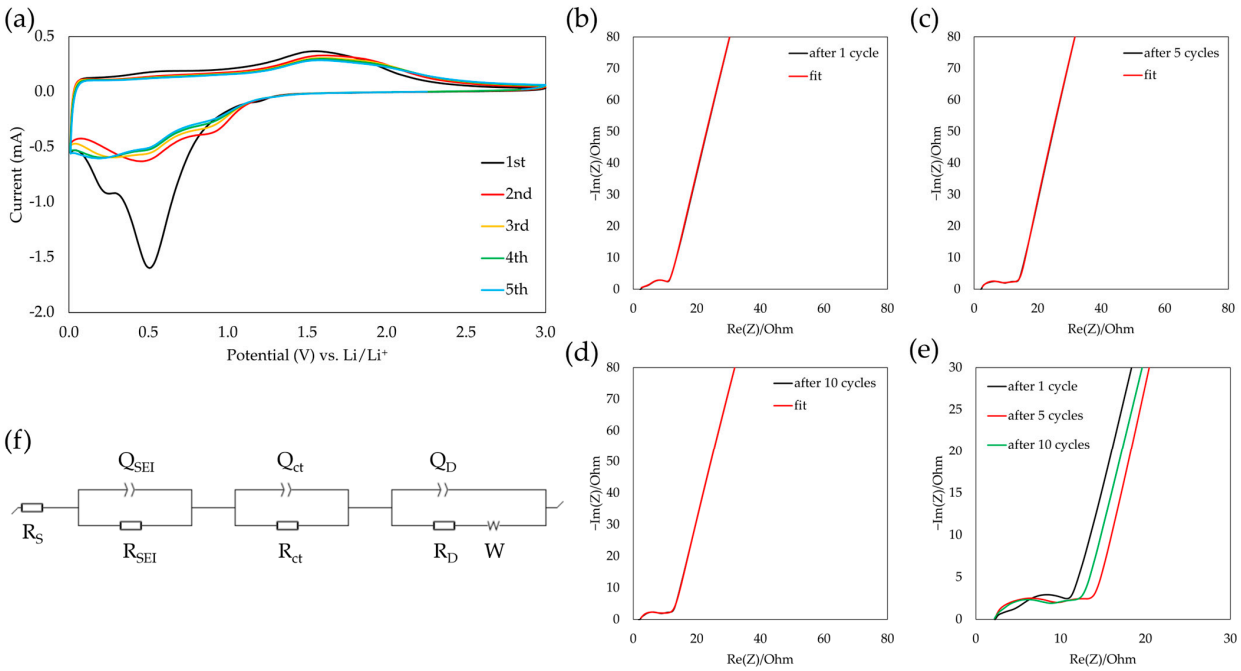

Figure 2. (**a**) CV curves at 0.1 mV s^{-1} in a potential range of 0.01–3 V vs. Li/Li^+, Nyquist plots of $(CrMnFeCoCu)_3O_4$ electrode and the corresponding equivalent circuit (**b**) after 1 cycle, (**c**) after 5 cycles, and (**d**) after 10 cycles; (**e**) Nyquist plots at different cycle number; (**f**) equivalent circuit fitting.

3.2.2. Electrochemical Impedance Spectroscopy

Electrochemical Impedance Spectroscopy (EIS) measurements were conducted on the prepared high-entropy oxide (HEO) electrode at a stable open circuit potential at the same state of charge (1.7 V) during different cycle numbers. Nyquist plots with equivalent circuit fitting were constructed to assess the evolution of its electrochemical behavior.

The same equivalent circuit (Figure 2f) was employed for all measurements at different cycle numbers to analyze the formation of the SEI layer during the cycling process, as was performed in [30]. A similar version of the equivalent circuit described in [15,23,29,47–49] was used to fit the EIS spectra. R_s, R_{ct}, R_{SEI}, and R_D represent the solution resistance, charge transfer resistance, SEI layer resistance, and diffusion resistance, respectively, while Q_{ct}, Q_{SEI}, and Q_D are interfacial constant phase elements for charge transfer, SEI layer, and Li-ion diffusion, respectively [15,16,29]. A Warburg element (s) was used for better describing the diffusion inside the cell.

The Nyquist plot of the electrode after the 1st discharge/charge cycle (Figure 2b) exhibited two semicircles at high and medium frequencies, representing the SEI layer impedance and charge transfer resistance, respectively. Li-ion diffusion in the electrode materials was represented with a sloping line in the low-frequency region.

After five discharge/charge cycles, the Nyquist plot (Figure 2c) of the electrode showed a similar shape with two semicircles and a sloping line. However, the first semicircle representing the SEI layer impedance had a larger diameter, indicating higher impedance (Table 3). This higher SEI layer impedance can be attributed to the initial formation of the SEI layer during the first cycles of the electrode. Conversely, the charge transfer resistance decreased during cycling, as shown in Figure 2e and Table 3. After 10 discharge–charge cycles, the shape of the Nyquist plot (Figure 2d) remained comparable to that observed after five cycles. However, the charge transfer resistance was higher and the SEI resistance was lower after 10 cycles. This observation aligns with the findings of [15], where the authors also reported an increase in SEI layer impedance in the first cycles and consequently its decrease due to the stabilization of the SEI layer.

Table 3. Estimated values of the parameters and their standard error of EIS fitting.

Parameters	After 1 Cycle		After 5 Cycles		After 10 Cycles	
	Estimated Value	Standard Error	Estimated Value	Standard Error	Estimated Value	Standard Error
R_S (Ohm)	1.582	0.1199	2.099	0.08994	2.253	0.03945
Q_{SEI} ($F\ s^{a_{SEI}-1}$)	83.09×10^{-6}	3.176×10^{-6}	18.65×10^{-6}	4.579×10^{-6}	0.7462×10^{-3}	59.86×10^{-6}
a_{SEI}	1	98.37×10^{-6}	0.7396	0.02129	0.7475	0.01667
R_{SEI} (Ohm)	3.335	0.08772	6.717	0.3391	4.121	0.1684
Q_{ct} ($F\ s^{a_{ct}-1}$)	3.73×10^{-3}	0.4309×10^{-3}	0.8871×10^{-3}	0.1049×10^{-3}	31.73×10^{-6}	3.855×10^{-6}
a_{ct}	0.3659	0.01401	0.6616	0.02349	0.734	0.01097
R_{ct} (Ohm)	7.371	0.2094	5.834	0.3368	6.488	0.1707
Q_D($F\ s^{a_D-1}$)	2.698×10^{-3}	11.1×10^{-6}	2.119×10^{-3}	8.368×10^{-6}	2.31×10^{-3}	5.394×10^{-6}
a_D	0.878	1.496×10^{-3}	0.9006	1.448×10^{-3}	0.8759	0.8391×10^{-3}
R_D (Ohm)	2.42×10^{-3}	0.04293	7.072	3.21	33.98	13.22
s (Ohm $s^{-1/2}$)	2189	90.79	1590	37.16	2073	41.68

3.2.3. Galvanostatic Cyclic Test

Figure 3a presents the voltage profile of the prepared HEO during galvanostatic charge/discharge at 100 mA g^{-1}. In the first discharge, a characteristic voltage profile for transition metal oxides is observed, featuring a plateau at an average potential of 0.5 V [15–17], consistent with the CV data, suggesting SEI layer formation due to electrolyte decomposition. The first charge profile displays a slope instead of a plateau in the 1.2 to 2 V range, aligning with the CV data. The dQ/dV plot (Figure 3b) reveals two main reactions during the initial discharge, mirroring the CV data. The discharge- and charge-specific capacities were 1140 and 650 mAh g^{-1}, respectively, resulting in a low

Coulombic efficiency of 58%, attributed to electrolyte decomposition and irreversible phase transformations, particularly amorphization [11,15,17,20,46]. In subsequent cycles, the voltage profiles maintained similar shapes, indicating remarkable reversibility and cycling stability. However, a slight decrease in specific capacity is observed until the 30th cycle (Figure 3c), reaching 512 mAh g^{-1}, a typical behavior for conversion materials. After this point, the capacity began to increase, possibly due to activation processes, structural rearrangements [15,16,26,30,33], or pulverization; particle size reduction can occur due to volume changes during the cycling process, leading to the formation of new surfaces that enhance overall capacity [50]. The dQ/dV plot reveals additional reactions starting at 0.28 V from the 30th cycle attributed to electrolyte degradation [15–17,20,29]. After 100 cycles, the initial charge capacity was completely restored to 676 mAh g^{-1}.

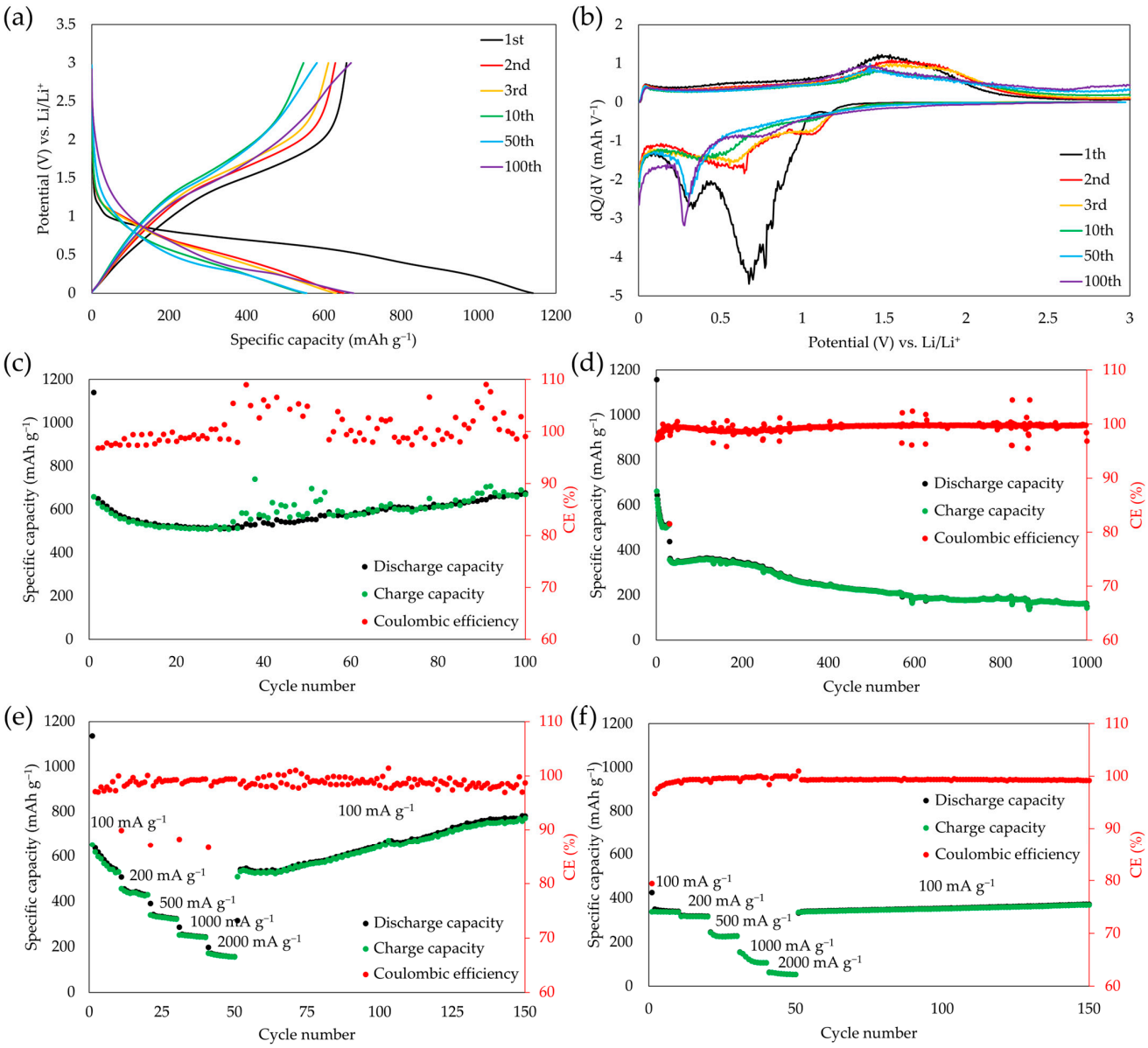

Figure 3. (**a**) Charge/discharge voltage profiles of HEO at 100 mA g^{-1}; (**b**) differential capacity plots of HEO at 100 mA g^{-1}; (**c**) cyclic stability test of HEO at 100 mA g^{-1}; (**d**) cyclic stability test of HEO at 500 mA g^{-1}; (**e**) rate capability test of HEO; (**f**) rate capability test of graphite.

The rate capability test (Figure 3e) demonstrated the electrochemical performance of the prepared HEOs at higher current densities. As current densities increased, specific capacities decreased due to diffusion limitations and polarization [25,51]. Specific capacities were

observed at 578, 442, 339, 254, and 168 mAh g^{-1} for current densities of 100, 200, 500, 1000, and 2000 mA g^{-1}, respectively. Decreasing the current density back to the initial value of 100 mA g^{-1} resulted in a regeneration of the specific capacity to 542 mAh g^{-1}. This capacity recovery, observed only in certain HEOs [11,19,21,23,30,46], is indicative of the material's unique electrochemical behavior. Subsequent cycles displayed a similar trend of capacity increase as observed in the cyclic stability test, with higher capacities of 772 mAh g^{-1} obtained compared to the initial cycles at the same current density. This phenomenon, observed in only a few HEOs [11,23,32,33], can be attributed to the high oxygen vacancy content in the structure. Compared to commercial graphite (Figure 3f, Table 4), the capacity ratio of HEO/graphite capacities increased with higher current densities, indicating that HEO is more efficient than graphite at higher current densities due to its superior rate capability. The HEO electrode exhibits 2 to 3 times higher specific capacities than graphite.

Table 4. Specific capacities of HEO and graphite at different current densities.

Material	Specific Capacities (mAh g^{-1}) at Current Densities (mA g^{-1})					
	100	**200**	**500**	**1000**	**2000**	**100**
HEO	577.6	441.7	339.1	254.2	167.5	772.9
Graphite	343.6	319.4	229.9	121.3	57.4	370.9
HEO/graphite capacity ratio	1.7	1.4	1.5	2.1	2.9	2.1

In cyclic stability testing (Figure 3d) at a current density of 500 mA g^{-1}, which included a 30-cycle formation process at 100 mA g^{-1} to activate the electrode, the HEO electrode exhibited moderate cyclic stability and specific capacity over 1000 cycles compared to other high-entropy oxides [16,19,22,23]. After 200 cycles, the capacity began to fade, likely due to electrode pulverization. A proportion of 80% (275 mAh g^{-1}) of the initial stable capacity (344 mAh g^{-1}) at 500 mA g^{-1} was achieved in the 312th cycle. Although a capacity retention of 80% in 300 cycles is commonly observed in HEOs, as summarized in [52], the final capacity after 1000 cycles at 500 mA g^{-1} decreased to 150 mAh g^{-1}, which is lower than in other high-entropy oxides. This behavior can be attributed to the fact that the average particle size of our HEO was higher than that in other studies, where nanoparticles were used. However, the moderate cyclic stability of the HEO can be attributed to its high entropy and amorphous structure, mitigating volume changes during cycling [15,20], compared to binary transitional metal oxides, even when using nanoparticles, such as in the case of Co_3O_4 [53].

Finally, we would like to state that, while the reversibilities of our materials rank among the top for traditional conversion materials, they cannot match the performance of state-of-the-art intercalation materials like NCM, LCO, or LFP. The mechanisms of intercalation and conversion differ significantly, each offering advantages and disadvantages. Improving reversibility, particularly in conversion materials, remains a critical goal driving our research efforts.

3.3. Post-Mortem Analysis

The post-mortem analysis revealed structural changes in the active material after 10 cycles. XRD analysis (Figure 4) showed phase transformation during the cycling process, where characteristic peaks of the HEO disappeared, and a new, unidentified small peak emerged at 3.12 $Å^{-1}$. This suggests amorphization of the HEO structure, contributing to its observed electrochemical performance that was discussed earlier. SEM analysis of the electrode surface before (Figure 5a,b) and after cycling (Figure 5d,e) revealed the formation of new surfaces, possibly arising from cracks induced by volume changes during cycling, causing particles to pulverize and create new active sites. However, cracks on the electrode surface may impede electrical contact, leading to capacity decline. The elemental distribution remained uniform, with no segregation observed (Figure 5c,f).

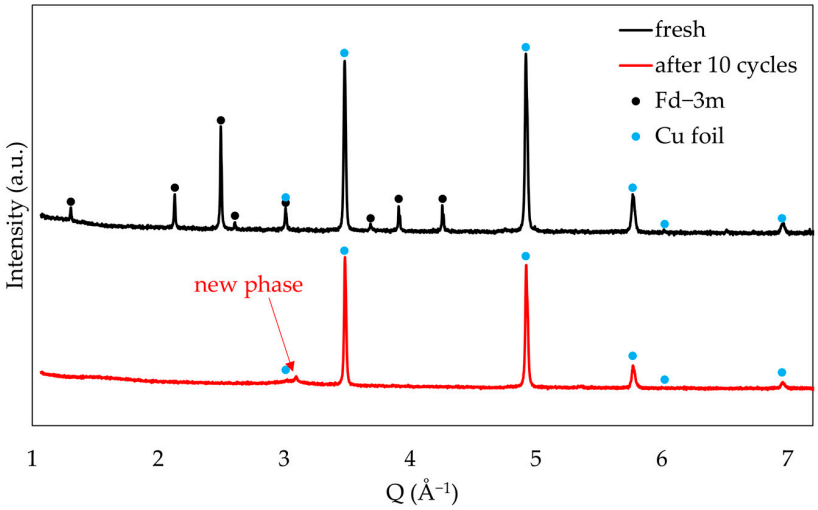

Figure 4. XRD of the electrodes before and after 10 cycles.

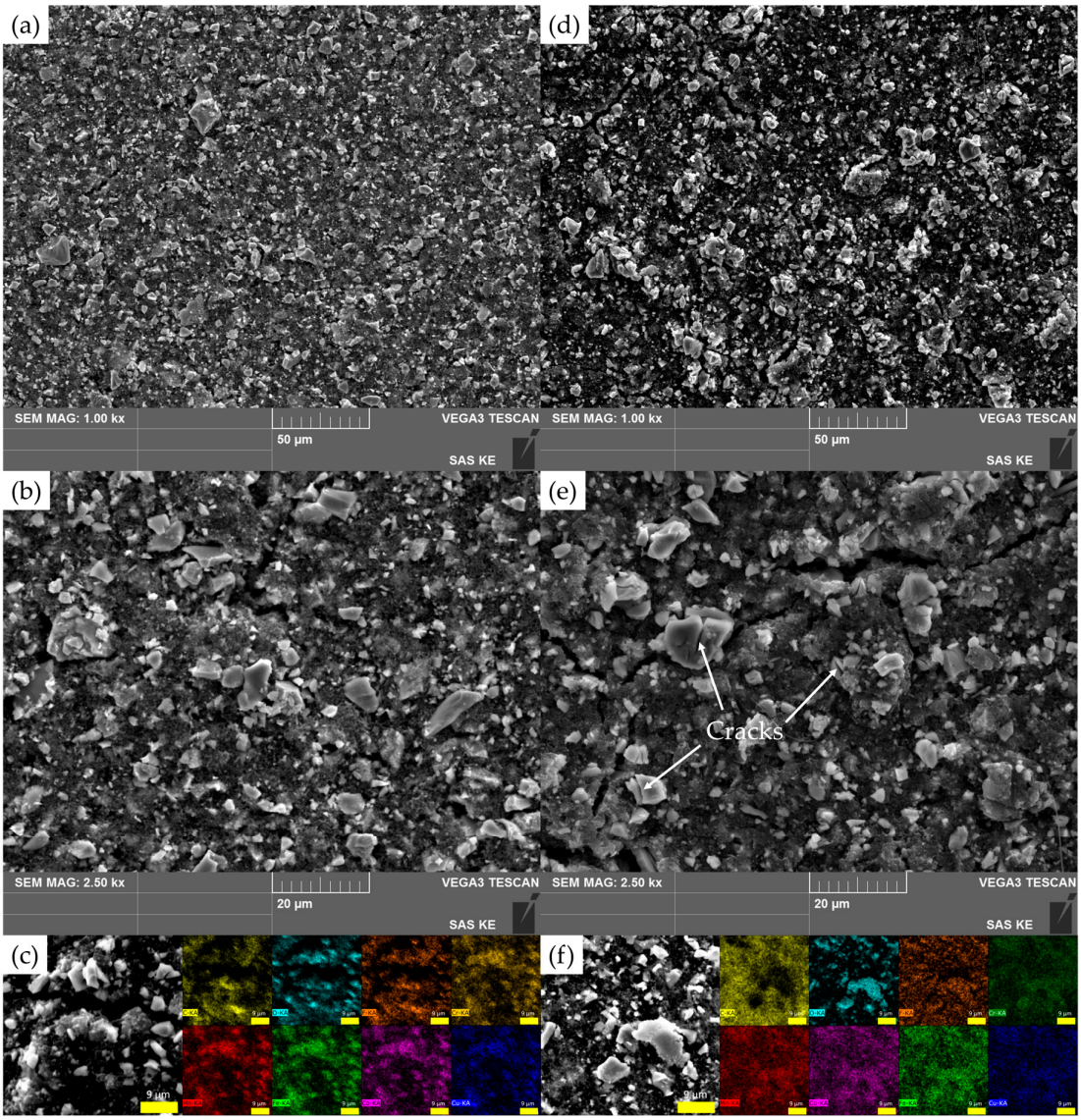

Figure 5. SEM micrographs of HEO electrodes (**a**,**b**) before and (**d**,**e**) after 10 cycles at 100 mA g^{-1}; EDS mapping of HEO electrodes (**c**) before and (**f**) after 10 cycles at 100 mA g^{-1}.

4. Conclusions

This study focused on the preparation of a high-entropy oxide of $(CrMnFeCoCu)_3O_4$ by arc melting a multicomponent alloy followed by high-temperature oxidation in an oxygen atmosphere. The resulting material exhibited a spinel oxide structure as the primary phase, accompanied by a minor amount of a secondary phase with a monoclinic structure.

The prepared high-entropy oxide $(CrMnFeCoCu)_3O_4$ was used in a half-cell lithium-ion battery configuration as an active electrode material and its performance was compared to commercial graphite. The results showed that the HEO/graphite capacity ratio increased with increasing current densities. This indicates that HEO exhibits higher efficiency than graphite at higher current densities, due to its superior ability to accommodate lithium ions during charge and discharge cycles. The tested half-cell showed moderate cyclic stability and maintained intermediate specific capacity over 1000 cycles.

The fresh electrode surface exhibited a uniform morphology, but post-mortem analysis revealed that the material experienced significant amorphization during the cycling process. However, the electrode surface remained compact even after 10 cycles, although cracks emerged on the surface of the powder particles. These cracks suggest the formation of new active surface areas, which may contribute to the observed capacity increase.

This research offers valuable insights into the potential of high-entropy oxide $(CrMnFeCoCu)_3O_4$ as a promising alternative to graphite in lithium-ion batteries, demonstrating capacity retention over extended cycling periods while maintaining initial discharge capacities.

Author Contributions: Conceptualization, L.O., D.C. and G.B. (Gabriela Baranová); methodology, L.O., D.C., G.B. (Gábor Bortel) and R.D.; validation, L.O., D.C. and G.B. (Gabriela Baranová); formal analysis, G.B. (Gábor Bortel), L.T. and M.H.; investigation, L.O., D.C., G.B. (Gábor Bortel) and R.D.; resources, M.H., B.B. and K.S.; data curation, D.C., G.B. (Gábor Bortel) and R.D.; writing—original draft preparation, L.O., D.C. and G.B. (Gabriela Baranová); writing—review and editing, L.O., D.C., G.B. (Gabriela Baranová), G.B. (Gábor Bortel), R.D., L.T., M.H., B.B. and K.S.; visualization, L.O. and D.C.; supervision, M.H., B.B. and K.S.; project administration, L.O., D.C. and L.T.; funding acquisition, L.T. and K.S. All authors have read and agreed to the published version of the manuscript.

Funding: This work was supported by the Slovak Research and Development Agency under the Contract no. APVV-20-0138 and APVV-20-0205, by the ELKH project 'Structure of materials used in energy storage' (Grant No. SA-89/2021). The research was supported by the Scientific Grant Agency of the Ministry of Education, Science, Research and Sport of the Slovak Republic and the Slovak Academy of Sciences VEGA project No. 2/0039/22 and the Technical University of Košice (Grant Number 05/TUKE/2023). This research was funded in part by the international projects EIG CONCERT-Japan/2021/215/EHSAL and M-ERA.NET 3/2022/235/H2MobilHydride.

Data Availability Statement: Data are contained within the article.

Conflicts of Interest: The authors declare no conflicts of interest.

References

1. Nitta, N.; Wu, F.; Lee, J.T.; Yushin, G. Li-Ion Battery Materials: Present and Future. *Mater. Today* **2015**, *18*, 252–264. [CrossRef]
2. Li, G.; Guo, S.; Xiang, B.; Mei, S.; Zheng, Y.; Zhang, X.; Gao, B.; Chu, P.K.; Huo, K. Recent advances and perspectives of microsized alloying-type porous anode materials in high-performance Li- and Na-ion batteries. *Energy Mater* **2022**, *2*, 200020. [CrossRef]
3. Wang, H.; Chen, S.; Fu, C.; Ding, Y.; Liu, G.; Cao, Y.; Chen, Z. Recent Advances in Conversion-Type Electrode Materials for Post Lithium-Ion Batteries. *ACS Mater. Lett.* **2021**, *3*, 956–977. [CrossRef]
4. Yu, S.-H.; Feng, X.; Zhang, N.; Seok, J.; Abruna, H.D. Understanding Conversion-Type Electrodes for Lithium Rechargeable Batteries. *Acc. Chem. Res.* **2018**, *51*, 273–281. [CrossRef] [PubMed]
5. Xu, H.; Li, H.; Wang, X. The Anode Materials for Lithium-Ion and Sodium-Ion Batteries Based on Conversion Reactions: A Review. *ChemElectroChem* **2023**, *10*, e2022011. [CrossRef]
6. Ma, J.; Huang, C. High entropy energy storage materials: Synthesis and application. *J. Energy Storage* **2023**, *66*, 107419. [CrossRef]
7. Wang, O.; Sarkar, A.; Li, Z.; Lu, Y.; Velasco, L.; Bhattacharya, S.S.; Brezesinski, T.; Hahn, H.; Breitung, B. High entropy oxides as anode material for Li-ion battery applications: A practical approach. *Electrochem. Commun.* **2019**, *100*, 121–125. [CrossRef]
8. Gao, Y.; Liu, Y.; Yu, H.; Zou, D. High-entropy oxides for catalysis: Status and perspectives. *Appl. Catal. A Gen.* **2022**, *631*, 118478. [CrossRef]

9. Zhu, H.; Xie, H.; Zhao, Y.; Dai, S.; Li, M.; Wang, X. Structure and magnetic properties of a class of spinel high-entropy oxides. *J. Magn. Magn. Mater.* **2021**, *535*, 168063. [CrossRef]
10. Li, H.; Zhou, Y.; Liang, Z.; Ning, H.; Fu, X.; Xu, Z.; Qiu, T.; Xu, W.; Yao, R.; Peng, J. High-Entropy Oxides: Advanced Research on Electrical Properties. *Coatings* **2021**, *11*, 628. [CrossRef]
11. Sarkar, A.; Velasco, L.; Wang, D.; Wang, Q.; Talasila, G.; de Biasi, L.; Kübel, C.; Brezesinski, T.; Bhattacharya, S.S.; Hahn, H.; et al. High entropy oxides for reversible energy storage. *Nat. Commun.* **2018**, *9*, 3400. [CrossRef]
12. Qiu, N.; Chen, H.; Yang, Z.; Sun, S.; Wang, Y.; Cui, Y. A high entropy oxide ($Mg_{0.2}Co_{0.2}Ni_{0.2}Cu_{0.2}Zn_{0.2}O$) with superior lithium storage performance. *J. Alloys Compd.* **2019**, *777*, 767–774. [CrossRef]
13. Wang, S.-Y.; Chen, T.-Y.; Kuo, C.-H.; Lin, C.-C.; Huang, S.-C.; Lin, M.-H.; Wang, C.-C.; Chen, H.-Y. Operando synchrotron transmission X-ray microscopy study on (Mg, Co, Ni, Cu, Zn)O high-entropy oxide anodes for lithium-ion batteries. *Mater. Chem. Phys.* **2021**, *274*, 125105. [CrossRef]
14. Yan, J.; Wang, D.; Zhang, X.; Li, J.; Du, Q.; Liu, X.; Zhang, J.; Qi, X. A high-entropy perovskite titanate lithium-ion battery anode. *J. Mater. Sci.* **2020**, *55*, 6942–6951. [CrossRef]
15. Wang, D.; Jiang, S.; Duan, C.; Mao, J.; Dong, Y.; Dong, K.; Wang, Z.; Luo, S.; Liu, Y.; Qi, X. Spinel-structured high entropy oxide $(FeCoNiCrMn)_3O_4$ as anode towards superior lithium storage performance. *J. Alloys Compd.* **2020**, *844*, 156158. [CrossRef]
16. Xiao, B.; Wu, G.; Wang, T.; Wei, Z.; Sui, Y.; Shen, B.; Qi, J.; Wei, F.; Zheng, J. High-entropy oxides as advanced anode materials for long-life lithium-ion Batteries. *Nano Energy* **2022**, *95*, 106962. [CrossRef]
17. Nguyen, T.X.; Patra, J.; Chang, J.K.; Ting, J.M. High entropy spinel oxide nanoparticles for superior lithiation-delithiation performance. *J. Mater. Chem. A* **2020**, *8*, 18963–18973. [CrossRef]
18. Huang, C.-Y.; Huang, C.-W.; Wu, M.-C.; Patra, J.; Nguyen, T.X.; Chang, M.-T.; Clemens, O.; Ting, J.-M.; Li, J.; Chang, J.-K.; et al. Atomic-scale investigation of Lithiation/Delithiation mechanism in High-entropy spinel oxide with superior electrochemical performance. *Chem. Eng.* **2021**, *420*, 129838. [CrossRef]
19. Chen, H.; Qiu, N.; Wu, B.; Yang, Z.; Sun, S.; Wang, Y. A new spinel high-entropy oxide $(Mg_{0.2}Ti_{0.2}Zn_{0.2}Cu_{0.2}Fe_{0.2})_3O_4$ with fast reaction kinetics and excellent stability as an anode material for lithium-ion batteries. *RSC Adv.* **2020**, *10*, 9736–9744. [CrossRef]
20. Duan, C.; Tian, K.; Li, X.; Wang, D.; Sun, H.; Zheng, R.; Wang, Z.; Liu, Y. New spinel high-entropy oxides $(FeCoNiCrMnXLi)_3O_4$ (X = Cu, Mg, Zn) as the anode material for lithium-ion batteries. *Ceram. Int.* **2021**, *47*, 32025–32032. [CrossRef]
21. Xiao, B.; Wu, G.; Wang, T.; Wei, Z.; Sui, Y.; Shen, B.; Qi, J.; Wei, F.; Meng, Q.; Ren, Y.; et al. High entropy oxides $(FeNiCrMnX)_3O_4$ (X = Zn, Mg) as anode materials for lithium ion batteries. *Ceram. Int.* **2021**, *47*, 33972–33977. [CrossRef]
22. Nguyen, T.X.; Tsai, C.-C.; Patra, J.; Clemens, O.; Chang, J.-K.; Ting, J.-M. Co-free high entropy spinel oxide anode with controlled morphology and crystallinity for outstanding charge/discharge performance in Lithium-ion batteries. *Chem. Eng. J.* **2022**, *430*, 132658. [CrossRef]
23. Kheradmandfard, M.; Minouei, H.; Tsvetkov, N.; Vayghan, A.K.; Kashani-Bozorg, S.F.; Kim, G.; Hong, S.I.; Kim, D.-E. Ultrafast green microwave-assisted synthesis of high-entropy oxide nanoparticles for Li-ion battery applications. *Mater. Chem. Phys.* **2021**, *262*, 124265. [CrossRef]
24. Lin, L.; Wang, K.; Azmi, R.; Wang, J.; Sarkar, A.; Botros, M.; Najib, S.; Ciu, Y.; Stenzel, D.; Su9kkurji, P.A.; et al. Mechanochemical synthesis: Route to novel rock-salt-structured high-entropy oxides and oxyfluorides. *J. Mater. Sci.* **2020**, *55*, 16879–16889. [CrossRef]
25. Chen, T.-Y.; Wang, S.-Y.; Kuo, C.-H.; Huang, S.-C.; Lin, M.-H.; Li, C.-H.; Chen, H.-Y.T.; Wang, C.-C.; Liao, Y.-F.; Lin, C.-C.; et al. In operando synchrotron X-ray studies of a novel spinel $(Ni_{0.2}Co_{0.2}Mn_{0.2}Fe_{0.2}Ti_{0.2})_3O_4$ high-entropy oxide for energy storage applications. *J. Mater. Chem. A* **2020**, *8*, 21756–21770. [CrossRef]
26. Marques, O.J.B.J.; Walter, M.D.; Timofeeva, E.V.; Segre, C.U. Effect of Initial Structure on Performance of High-Entropy Oxide Anodes for Li-Ion Batteries. *Batteries* **2023**, *9*, 115. [CrossRef]
27. Wang, X.L.; Jin, E.M.; Sahoo, G.; Jeong, S.M. High-Entropy Metal Oxide $(NiMnCrCoFe)_3O_4$ Anode Materials with Controlled Morphology for High-Performance Lithium-Ion Batteries. *Batteries* **2023**, *9*, 147. [CrossRef]
28. Zheng, Y.; Wu, X.; Lan, X.; Hu, R. A Spinel $(FeNiCrMnMgAl)_3O_4$ High Entropy Oxide as a Cycling Stable Anode Material for Li-Ion Batteries. *Processes* **2022**, *10*, 49. [CrossRef]
29. Shin, D.; Chae, S.; Park, S.; Seo, B.; Choi, W. Rational engineering of high-entropy oxides for Li-ion battery anodes with finely tuned combustion syntheses. *NPG Asia Mater.* **2023**, *15*, 54. [CrossRef]
30. Xiao, B.; Wu, G.; Wang, T.; Wei, Z.; Xie, Z.; Sui, Y.; Qi, J.; Wei, F.; Zhang, X.; Tang, L.; et al. Enhanced Li-Ion Diffusion and Cycling Stability of Ni-Free High-Entropy Spinel Oxide Anodes with High-Concentration Oxygen Vacancies. *ACS Appl. Mater. Interfaces* **2023**, *15*, 2792–2803. [CrossRef]
31. Sun, Z.; Zhao, Y.; Sun, C.; Ni, Q.; Wang, C.; Jin, H. High entropy spinel-structure oxide for electrochemical application. *J. Chem. Eng.* **2022**, *431*, 133448. [CrossRef]
32. Zhao, J.; Yang, X.; Huang, Y.; Du, F.; Zeng, Y. Entropy Stabilization Effect and Oxygen Vacancies Enabling Spinel Oxide Highly Reversible Lithium-Ion Storage. *ACS Appl. Mater. Interfaces* **2021**, *13*, 58674–58681. [CrossRef]
33. Yang, X.; Wang, H.; Song, Y.; Liu, K.; Huang, T.; Wang, X.; Zhang, C.; Li, J. Low-Temperature Synthesis of a Porous High-Entropy Transition-Metal Oxide as an Anode for High-Performance Lithium-Ion Batteries. *ACS Appl. Mater. Interfaces* **2022**, *14*, 26873–26881. [CrossRef] [PubMed]

34. Luo, X.-F.; Patra, J.; Chuang, W.-T.; Nguyen, T.X.; Ting, J.-M.; Li, J.; Pao, C.-W.; Chang, J.-K. Charge–Discharge Mechanism of High-Entropy Co-Free Spinel Oxide Toward Li^+ Storage Examined Using Operando Quick-Scanning X-ray Absorption Spectroscopy. *Adv. Sci.* **2022**, *9*, 2201219. [CrossRef] [PubMed]
35. Patra, J.; Nguyen, T.X.; Tsai, C.-C.; Clements, O.; Li, J.; Pal, P.; Chan, W.K.; Lee, C.-H.; Chen, H.-Y.-T.; Ting, J.-M.; et al. Effects of Elemental Modulation on Phase Purity and Electrochemical Properties of Co-free High-Entropy Spinel Oxide Anodes for Lithium-Ion Batteries. *Adv. Funct. Mater.* **2022**, *32*, 2110992. [CrossRef]
36. Toby, B.H.; Von Dreele, R.B. GSAS-II: The genesis of a modern open-source all purpose crystallography software package. *J. Appl. Crystallogr.* **2013**, *46*, 544–549. [CrossRef]
37. Toby, B.H. EXPGUI, a graphical user interface for GSAS. *J. Appl. Crystallogr.* **2004**, *34*, 210–213. [CrossRef]
38. Otto, F.; Yang, Y.; Bei, H.; George, E.P. Relative effects of enthalpy and entropy on the phase stability of equiatomic high-entropy alloys. *Acta Mater.* **2013**, *61*, 2628–2638. [CrossRef]
39. Katsube, R.; Luo, L.; Nakano, K.; Narumi, T.; Yasuda, H. Solidification sequence of CrMnFeCoCu dual-FCC multicomponent alloy. *Scr. Mater.* **2023**, *231*, 115459. [CrossRef]
40. Miracle, D.B.; Senkov, O.N. A critical review of high entropy alloys and related concepts. *Acta Mater.* **2017**, *122*, 448–511. [CrossRef]
41. Dippo, O.F.; Vecchio, K.S. A universal configurational entropy metric for high-entropy materials. *Scr. Mater.* **2021**, *201*, 113974. [CrossRef]
42. Wu, Z.; Troparevsky, M.C.; Gao, Y.F.; Morris, J.R.; Stocks, G.M.; Bei, H. Phase stability, physical properties and strengthening mechanism of concentrated solid solution alloys. *Curr Opin Solid State Mater Sci.* **2017**, *21*, 267–284. [CrossRef]
43. He, X.; Zhang, Z.; Qiao, T.; Liu, H.; Jiang, X.; Xing, T.; Wang, S. Nanocrystalline $(CrMnFeCoCu)_3O_4$ High/Entropy Oxide for Efficient Oxygen Evolution Reaction. *ACS Appl. Nano Mater.* **2023**, *6*, 19573–19580. [CrossRef]
44. Fracchia, M.; Coduri, M.; Chigna, P.; Anselmi-Tamburini, U. Phase stability of high entropy oxides: A critical review. *J. Eur. Ceram. Soc.* **2024**, *44*, 585–594. [CrossRef]
45. Liu, B.-J.; Yin, T.-H.; Lin, Y.-W.; Chang, C.-W.; Yu, H.-C.; Lim, Y.; Lee, H.; Choi, C.; Tsai, M.-K.; Choi, Y. A Cost-Effective, Nanoporous, High-Entropy Oxide Electrode for Electrocatalytic Water Splitting. *Coatings* **2023**, *13*, 1461. [CrossRef]
46. Ghigna, P.; Airoldi, L.; Fracchia, M.; Callegari, D.; Anselmi-Tamburini, U.; D'Angelo, P.; Pianta, N.; Ruffo, R.; Cibin, G.; Oliveira de Souza, D.; et al. Lithiation Mechanism in High-Entropy Oxides as Anode Materials for Li-Ion Batteries: An Operando XAS Study. *ACS Appl. Mater. Interfaces* **2020**, *12*, 50344–50354. [CrossRef] [PubMed]
47. Chung, S.-H.; Wu, Y.-H.; Tseng, Y.-H.; Nguyen, T.X.; Ting, J.-M. High Entropy Oxide $(CrMnFeNiMg)_3O_4$ with Large Compositional Space Shows Long-Term Stability as Cathode in Lithium-Sulfur Batteries. *Chem. Sus. Chem.* **2023**, *16*, e202300135. [CrossRef]
48. Kazda, T.; Capková, D.; Jaššo, K.; Fedorková Straková, A.; Shembel, E.; Markevich, A.; Sedlaříková, M. Carrageenan as an Ecological Alternative of Polyvinylidene Difluoride Binder for Li-S Batteries. *Materials* **2021**, *14*, 5578. [CrossRef]
49. Capková, D.; Knap, V.; Fedorková Straková, A.; Stroe, D.-I. Analysis of 3.4 Ah lithium-sulfur pouch cells by electrochemical impedance spectroscopy. *J. Energy Chem.* **2022**, *72*, 318–325. [CrossRef]
50. Kim, H.; Choi, W.; Yoon, J.; Um, J.H.; Lee, W.; Kim, J.; Cabana, J.; Yoon, W.-S. Exploring Anomalous Charge Storage in Anode Materials for Next-Generation Li Rechargeable Batteries. *Chem. Rev.* **2020**, *120*, 6934–6976. [CrossRef]
51. Heubner, C.; Schneider, M.; Michaelis, A. Diffusion-Limited C-Rate: A Fundamental Principle Quantifying the Intrinsic Limits of Li-Ion Batteries. *Adv. Energy Mater.* **2019**, *10*, 1902523. [CrossRef]
52. Qu, J.; Buckingham, M.A.; Lewis, D.J. High-entropy materials for electrochemical energy storage devices. *Energy Adv.* **2023**, *2*, 1565–1590. [CrossRef]
53. Wu, Z.-S.; Ren, W.; Wen, L.; Gao, L.; Zhao, J.; Chen, Z.; Zhou, G.; Li, F.; Cheng, H.-M. Graphene Anchored with Co_3O_4 Nanoparticles as Anode of Lithium Ion Batteries with Enhanced Reversible Capacity and Cyclic Performance. *ACS Nano* **2010**, *4*, 3187–3194. [CrossRef] [PubMed]